IEEE Access
Multidisciplinary ⋮ Rapid Review ⋮ Open Access Journal

Received 19 October 2024, accepted 26 November 2024, date of publication 18 December 2024, date of current version 27 December 2024.

Digital Object Identifier 10.1109/ACCESS.2024.3514102

RESEARCH ARTICLE

Structural Design Optimization of Tidal Current Turbine Blades Based on Structural Safety Factors

HAECHANG JEONG [1], **(Member, IEEE), AND CHANGJO YANG** [2]
[1]Ocean Fluid Machinery Laboratory, Mokpo National Maritime University, Mokpo 58628, Republic of Korea
[2]Division of Marine Engineering, Mokpo National Maritime University, Mokpo 58628, Republic of Korea

Corresponding author: Changjo Yang (cjyang@mmu.ac.kr)

This work was supported by the National University Development Project through the National Research Foundation of Korea funded by the Ministry of Education.

ABSTRACT To commercialize tidal power turbines, it is essential to ensure high efficiency and structural integrity. In this study, a rule of mixture design approach is applied to the turbine blades, and the optimal structural design is determined based on criteria for structural safety and mass reduction. The blades for megawatt tidal power turbines are hydrodynamically designed using blade element momentum (BEM) theory, and made of composite materials—glass fiber-reinforced plastics and carbon fiber-reinforced plastics. The layered structure of the composite is designed to meet the failure criteria under both normal and extreme operating conditions, and the structural integrity of the layered blade design is verified through finite element modeling, adhering to failure theories based on limit criteria, interaction criteria, and separation mode criteria. Additionally, a genetic algorithm is employed to calculate the optimal structural design model, setting the shell and spar cap as design parameters and performing load analysis according to the stacking reduction ratio. Using this process, the candidates for the optimal design model are selected based on the assigned weights on the Pareto frontier. As a result, the mass of the blade is reduced by 23.6% compared to the initial model, and the structural safety factors meet all the failure criteria under extreme load conditions, thereby ensuring a broad operational range for the tidal power turbines.

INDEX TERMS Failure criterion, genetic algorithm, optimal structure design, structural safety factor, tidal current turbine blades.

NOMENCLATURE

BEM	Blade element momentum.
FRP	Fiber-reinforced plastic.
MW	Mega-watt.
GA	Genetic algorithm.
SRR	Stacking reduction ratio.
NREL	National renewable energy laboratory.
TE	Trailing edge.
LE	Leading edge.
UD	Uni-directional.
DB	Double-bias.
QA	Quadra-axial.
NS	Non symmetry.
IRF	Inverse reserve factor.
NOC	Normal operating condition.
EOC	Extreme operating condition.
a	Axial flow induction factor.
a'	Tangential flow induction factor.

The associate editor coordinating the review of this manuscript and approving it for publication was Frederico Guimarães.

I. INTRODUCTION

The energy produced by tidal current turbines is predictable due to the regular and consistent patterns of tidal flows [1]. These turbines demonstrate greater output and structural load than wind turbines, because of the higher density of seawater. A key factor in their performance is the rotor blades, which serve as the main components for both power generation and structural load. Consequently, these blades must be designed to meet stringent performance and durability standards [2]. Blade design for tidal turbines must account for variations in power output and mechanical loads resulting from environmental factors such as water depth and current velocity at the installation site. Therefore, the development of advanced and robust blade design technologies is crucial for establishing a competitive and efficient tidal turbine system.

Rotor blades are exposed to high thrust and bending moments in extreme environments for extended period, necessitating robust hydrodynamic and structural designs to ensure stable operation and straightforward maintenance [3]. To effectively respond to hydrodynamic behavior, blades are required to be lightweight and strong. As a result, high-strength, high-stiffness composites such as glass fiber-reinforced plastics (GFRP) for large wind turbine rotor blades and carbon fiber-reinforced plastics (CFRP) for tidal power rotor blades are essential [4], [5]. Several studies have explored material deformation and damage under varying loads, confirming the economic feasibility and structural safety of using GFRP versus CFRP in tidal power rotor blades [6], [7].

The structural safety of these composite materials requires precise structural analysis that accounts for the stacking direction and pattern in each section. Flawed designs can cause failures across the turbine system, making structural integrity assessments critical during the design process. Structural safety is confirmed through standard load tests as defined by the International Electrotechnical Commission (IEC) 62600 or industry guidelines, which typically involve performance tests of structural units to detect potential damage. Despite these measures, damage instances have still been reported. For example, a 35 kW tidal turbine developed by Verdant Power experienced buckling damage to the blade shell and spar cap in New York's East River, while a 100 kW tidal power turbine made from GFRP by OceanSpace in Korea suffered damage at the transition from the in-board to mid-board sections of the blade root.

These incidents highlight the need for more advanced research into damage assessment using finite element (FE) models before conducting structural performance tests [8]. Currently, such research primarily focuses on wind turbine rotor blades and small to medium-scale tidal power turbines [9], [10]. Given the increased structural challenges in large-scale tidal power turbines due to augmented self-weight and loads, further studies on the structural safety of rotor blades are essential. Therefore, this study focused on the design of a large-scale tidal current turbine and the evaluation of its structural safety. Additionally, a risk assessment mechanism proposed during the manufacturing stage aims to optimize maintenance decisions [11].

This study proposes an optimal structural design method using genetic algorithms (GA) to ensure structural safety and to develop a systematic design system for mega-watt (MW)-class rotor blades for tidal power generation. The internal structure of these rotor blades is divided into the shell, spar cap, and shear web, which support most of the load, and they are designed in layers that reflect the characteristics of the structure. The structural properties of the blades are determined by the arrangement of internal structures and stacking methods, including material type, lamination thickness, and lamination angle. Additionally, to structural safety, a mixed design using composite materials GFRP and CFRP was chosen to ensure economic efficiency through blade mass reduction [12].

The blade FE model converts local thrust and torque under normal and extreme load conditions into surface pressure coefficients, which are then inputted for load analysis. This analysis provides comprehensive evaluations of blade tip deflections, strain, fiber breakage, and inter-fiber damage to assess structural safety. Furthermore, the FE model for MW turbines analyzes the results of load analysis based on various failure criteria, including limit state, interaction, and separation mode criteria. By applying various failure criteria, the load analysis results can enhance reliability compared to those of existing studies [13], [14], [15].

To derive the optimal structural design model for the rotor blades, a GA was applied, setting design parameters, variables, objective functions, and constraints. Reference [16] utilized the Pareto frontier of a genetic algorithm to calculate the commercial point to enhance the performance of the Savonius wind turbine. Similarly, [17] conducted an optimal design of a centrifugal pump inducer using the TOPSIS technique, which is based on the similarity to the ideal solution. This study also identified candidates for the optimal structural design model based on assigned weights along the Pareto frontier. Furthermore, to evaluate structural safety concerning the stacking reduction ratio for each blade section, both drop-off and linear design methods were utilized to assess potential damage.

II. PRELIMINARIES

The design of rotor blades for tidal current turbines is based on hydrodynamic performance calculations using the blade element momentum (BEM) theory [18]. In the initial design stage, the selection of composite materials for internal structures such as the blade shell, spar cap, and shear web is guided by their structural properties. The fabrication processes and structures are customized such that the layers are stacked outward to the blade for the initial geometry and inward to the blade for the internal structure of the blade to ensure that the stacking does not impair performance. The ANSYS-ACP, a tool widely applied in layered design in numerous studies, was utilized [5], [19], [20]. This section discusses both the hydrodynamic and structural designs based on the materials.

A. HYDRODYNAMIC DESIGN

The geometry of the blade is designed as a three-dimensional assembly of two-dimensional cross-sections, spaced incrementally from the hub to the tip [21]. Initially, design parameters such as rated power, power coefficient, fluid density, design current velocity, rotor diameter, and design rotational speed are established based on current direction and velocity data from the proposed installation site. Given that the installation capacity of tidal current turbines is constrained by water depth, we designed an MW-class horizontal-axis turbine blade for an average water depth of 45 m. The rotor blades, configured as three-blade, upwind type with a length advantage, were designed with a rated current velocity of 2.5 m/s. For the rotor blade diameter (D_{rotor}), we adopted a power coefficient ($C_{p,estimated}$) of 0.45 and a power system efficiency (η) of 0.93. P_{rated} represents the rated power, and V_{rated} and ρ_{water} represent the rated current velocity, and seawater density, respectively. The design tip speed ratio is denoted by λ_{design}, and the inflow velocity of the fluid is represented by V_{inflow}.

$$D_{rotor} = \sqrt{\frac{8P_{rated}}{\eta C_{p,estimated}\rho_{water}\pi V_{rated}^{3}}} \tag{1}$$

$$RPM = 60\left(\frac{V_{design}}{\pi D_{rotor}}\right)\lambda_{design} \tag{2}$$

$$\lambda_{design} = \frac{\pi RPMD_{rotor}}{60V_{inflow}} \tag{3}$$

TABLE 1. Design specifications for the rotor blade.

Design parameter	Unit	Value
Rated power	MW	1.0
Rated current velocity	m/s	2.5
Rotor blade diameter	m	19.8
Swept area of blade	m^2	307.9
Power efficiency	%	44.8
Cut-in / cut-out	m/s	1.5 / 3.3
Hydrofoil	-	NREL S814

Table 1 details the design specifications for the MW-class tidal current turbine. The hydrofoil utilized in this study is the NREL S814, chosen for its suitability in tidal applications owing to its thicker chord and root-side shape relative to other models in the S-series [22]. The S814 hydrofoil has been extensively validated through multiple experiments [23] and empirical testing on tidal current turbines at the Bay of Fundy, UK [24], [25].

B. MATERIAL PROPERTIES

The rotor blades are constructed from FRP, which provides the necessary strength and rigidity for dependable operation and maintenance. While most wind turbine blades maintain structural integrity, often constructed from GFRP alone [26], GFRP, despite its high impact and compressive strengths owing to its high density, is heavy and lacks elasticity. In contrast, CFRP offers superior elasticity and strength, as well as is corrosion-resistant, making it particularly advantageous for tidal current turbine blades that must endure extreme conditions. Incorporating CFRP to reduce the limitations of GFRP can decrease the mass of the rotor blade and enhance its structural safety, although comprehensive data on turbine blades for tidal power remains scarce, with previous research primarily focusing on singular composite materials [27].

In this study, we developed a rule of mixtures for designing blades with multiple composite materials, which is recognized as one of the optimal design methods for composites. According to this rule, when composite materials are layered perpendicular to the direction of the load acting on the blade, the original strength of the blade can increase by 10%. This theory has been applied in various research studies [28].

Table 2 illustrates the mechanical properties of the composite materials used in the blades for this study, which were applied in testing composite specimens and constructing an underwater turbine [13]. For the core materials used in the sandwich composites, this study referenced research on blades for a 1.5-MW-class tidal current turbine [6].

TABLE 2. Mechanical properties of the composite materials [6], [13].

Property	GFRP	CFRP	Core
Density (kg/m^3)	2000	1580	65
Longitudinal modulus (GPa)	45	156	0.44
Transverse modulus (GPa)	10	9.3	0.044
Major Poisson's ratio	0.3	0.3	0.30
In-plane shear modulus (GPa)	5	5.5	-
Longitudinal tensile strength (MPa)	1100	2500	0
Transverse tensile strength (MPa)	35	759	5.3
Longitudinal compressive strength (MPa)	675	2078	0
Transverse compressive strength (MPa)	120	165	5.3

C. STRUCTURAL DESIGN

The design approaches for rotor blades using composite materials have evolved, addressing not only structural concepts but also material selection and manufacturing processes as blade dimensions have increased [29]. Composite materials are integrated into the blade's internal structure, taking into account the supported load, with considerations for structural safety and cost-efficiency.

The basic structure of the blade is divided into the outer shell, inner shear web, spar cap, and foam core, as illustrated in Fig. 1. The layering of the structure is determined by the characteristics of the suction and pressure sides of the blade's cross-section.

Table 3 presents the materials and lay-up configurations of the internal components of the blade, which are categorized into three types: two configurations involving GFRP

TABLE 3. Lay-up configurations for different components.

Component	Material	Lay-up
Shell	GFRP	QA(0°/90°/±45°/Core)$_{NS}$
Shear web, TE, TE panel	GFRP	DB(±45°/Core)$_{NS}$
LE, spar cap	CFRP	UD(0°)

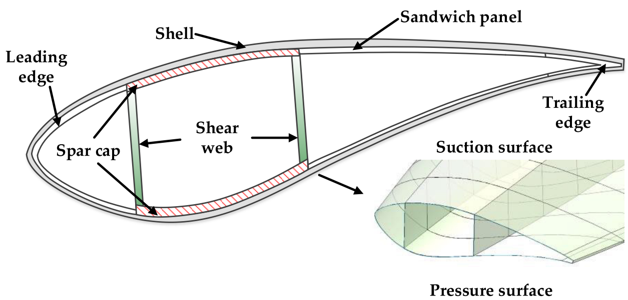

FIGURE 1. Cross-sectional schematic of the internal structure of the rotor blade.

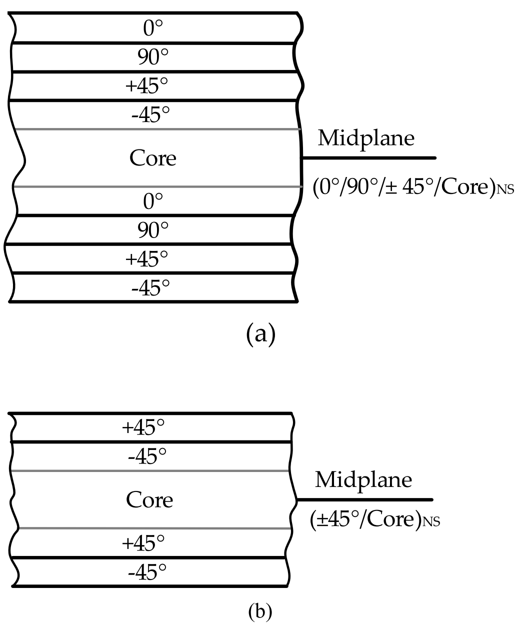

FIGURE 2. Composite material lay-up sequence and fiber angle direction in the finite-element model: (a) GFRP sandwich structural design(shell); (b) GFRP sandwich structural design(shear web, TE, TE panel).

and one involving CFRP. The spar cap and leading edge, which are subject to concentrated flapwise bending loads, are layered unidirectionally with stiff, lightweight CFRP to enhance rigidity.

Fig. 2 shows two GFRP-based lay-ups. The shell features a sandwich structure with quadra-axial (QA) glass fibers as depicted in Fig. 2(a), designed to maintain shape and handle torsional loads, while the core layer enhances flexural rigidity to improve buckling resistance. The shear web, trailing edge, and trailing edge panels, as shown in Fig. 2(b), are designed with a double-bias (DB) sandwich structure to support shear loads.

III. METHODOLOGY

A. FINITE-ELEMENT MODEL AND LOAD DISTRIBUTION

The blade's FE model and loads are calculated based on BEM theory [30], and the load values are input on the blade surface. Furthermore, we coupled commercial software ANSYS's FE code with the ANSYS optimization tool to ensure the reproducibility of the design and the reliability of the analysis [20], [26], [31].

This study also applied Prandtl's tip-loss model to account for the tip loss due to the rotation of the rotor blade in the geometry design. Fig. 3 shows the BEM theory applied to a blade element at radius r with thickness dr. Owing to the rotation of the turbine blades, the angular velocity of the flow increased from Ω to $\Omega + \omega$, and the flow velocity (V_1) and the relative resultant velocity (V_r) are calculated using (4) and (5), respectively.

$$V_1 = (\Omega + \omega/2)\,\mathrm{r} = \Omega \mathrm{r}(1+a') \tag{4}$$

$$V_r = \sqrt{V_1^2(1-a)^2 + \Omega^2 r^2 (1+a')^2} \tag{5}$$

The maximum stress and maximum strain theories, which are utilized not only in the failure evaluation of composite materials but also in steel assessments, represent key approaches within the limit criterion. This criterion facilitates the determination of failure strength and mode by comparing the stress components to the maximum tensile, compressive, and shear strengths of the stacked layers. However, it is a conservative criterion, as it does not account for the interrelationships between stress components. In contrast, the interaction criterion enables the detection of inter-fiber failure by considering the relationships among all stress and strain components. Using a single quadratic equation and a tensor polynomial equation, this criterion establishes the presence of failure when these equations are satisfied. This method is broadly utilized to predict the failure of orthotropic composite materials. The Tsai-Wu failure theory, an example of the interaction criteria, is formulated as shown in (6). A failure index value of ≥ 1 indicates the occurrence of failure in the composite material. The coefficient F_{ij} in the Tsai-Wu failure theory, which relates to the material strength of the composite, is expressed in (7) and (8) for the plane stress state of orthotropic composite materials.

$$F_i\sigma_i + F_{ij}\sigma_{ij} \leq 1 \quad (i, j = 1, 2, \cdots, 6) \tag{6}$$

$$\mathrm{F}_1\sigma_1 + \mathrm{F}_2\sigma_2 + 2\mathrm{F}_{12}\sigma_1\sigma_2 + \mathrm{F}_{11}\sigma_1^2 + \mathrm{F}_{22}\sigma_2^2 + \mathrm{F}_{66}\sigma_6^2 = 1 \tag{7}$$

$$\mathrm{F}_1 = \left(\frac{1}{\mathrm{X_T}} - \frac{1}{|\mathrm{X_T}|}\right), \mathrm{F}_2 = \left(\frac{1}{\mathrm{Y_T}} - \frac{1}{|\mathrm{Y_T}|}\right), \mathrm{F}_{11} = \frac{1}{\mathrm{X_T}\,|\mathrm{X_C}|},$$
$$\mathrm{F}_{22} = \frac{1}{\mathrm{Y_T}\,|\mathrm{Y_C}|}, \mathrm{F}_{66} = \frac{1}{\mathrm{S}^2}, \mathrm{F}_{12} = 0 \tag{8}$$

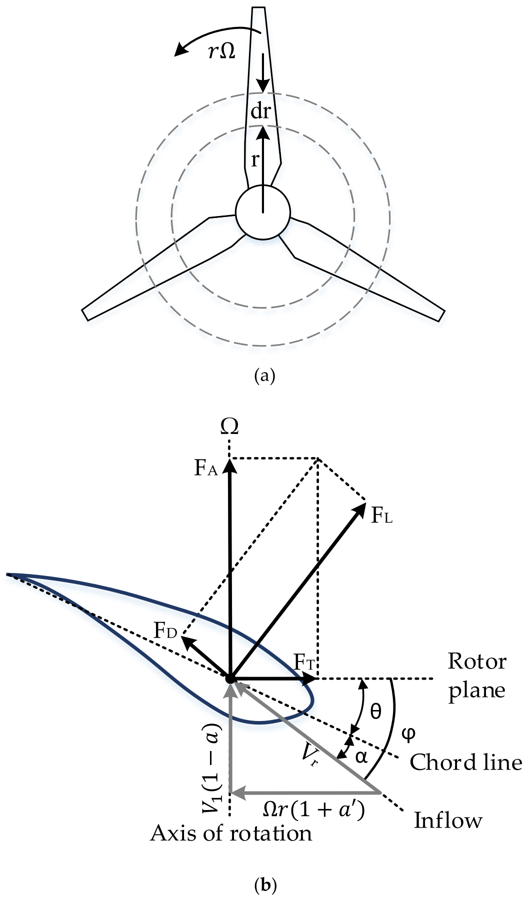

FIGURE 3. Schematic of rotor BEM theory: (a) annular plane for discretization; (b) hydrodynamic velocity and forces on a blade cross section.

Puck's failure theory, which embodies the separation mode criterion, combines the advantages of the limit and interaction criteria. It enables the evaluation of both fiber and inter-fiber failures in composite materials. Moreover, this theory allows for predicting failure modes by examining the correlations among stresses. Reference [33] introduces an evaluation method based on the angle of the fracture surface. Equation (9) defines the fiber failure index within the Puck failure criterion, incorporating parameters dependent on the fracture surface angle: p_{vp}^{+}, p_{vp}^{-}, and p_{vv}^{-}. R_{vv}^{A} is the resistance of the active surface against fractures caused by vertical shear stress, and τ_{21c} represents the shear stress at the transition point of the fracture curve.

$$S = \varepsilon_1 + \frac{v_{f12}}{E_{f1}} m_{\sigma f}\sigma_2 \geq 0 \tag{9}$$

$$p_{vp}^{+} = -\left(\frac{d\tau_{21}}{d\sigma_2}\right)_{\sigma_2=0} \; of\ (\sigma_2, \tau_{21})\ curve, \sigma_2 \geq 0 \tag{10}$$

$$p_{vp}^{-} = -\left(\frac{d\tau_{21}}{d\sigma_2}\right)_{\sigma_2=0} \; of\ (\sigma_2, \tau_{21})\ curve,\ \sigma_2 \leq 0 \tag{11}$$

$$R_{vv}^{A} = \frac{Y_C}{2(1+p_{vv}^{-})} = \frac{S_{21}}{2p_{vp}^{-}}\left(\sqrt{1+2p_{vp}^{-}\frac{Y_C}{S_{21}}}-1\right) \tag{12}$$

$$p_{vv}^{-} = p_{vv}^{-}\frac{R_{vv}^{A}}{S_{21}} \tag{13}$$

$$\tau_{21c} = S_{21}\sqrt{1+2p_{vv}^{-}} \tag{14}$$

Table 4 details the equations and conditions necessary to compute the failure index for each failure mode. ε_{1T} and ε_{1C} represent the tensile and compressive strains, respectively, of the unidirectional fiber layer; ε_1 represents the strain in this layer. The Poisson's ratio and elastic modulus of the fibers are represented by v_{f12} and E_{f1}, respectively; $m_{\sigma f}$ is the mean stress magnification constant for vertical stresses; σ_2 represents the vertical stress component; γ_{21} and τ_{21} represent the shear strain and stress, respectively, of the unidirectional layer; S_{21} represents the shear fracture strength perpendicular and parallel to the fibers; Y_T and Y_C represent the tensile and compressive fracture strengths, respectively, perpendicular to the fibers; and σ_{1D} represents the stress value determined through linear regression.

TABLE 4. Conditions for the Puck failure criterion [33].

Failure mode	Failure condition	Condition for validity
Fiber failure in tension	$\frac{S}{\varepsilon_{1T}} = 1$	$S \geq 0$
Fiber failure in compression	$\frac{1}{\varepsilon_{1C}}\left\lvert\left(\varepsilon_1 + \frac{\gamma_{f12}}{E_{f1}}m_{\sigma f}\sigma_2\right)\right\rvert + 10{\gamma_{21}}^2 = 1$	$S < 0$
Matrix failure mode A for transverse tension	$\sqrt{\left(\frac{\tau_{21}}{S_{21}}\right)^2 + \left(1 - p_{vp}^{+}\frac{Y_T}{S_{21}}\right)^2\left(\frac{\sigma_2}{Y_T}\right)^2} + p_{vp}^{+}\frac{\sigma_2}{S_{21}} + \frac{\sigma_1}{\sigma_{1D}} = 1$	$\sigma_2 \geq 0$
Matrix failure mode B for Moderate transverse compression	$\frac{1}{S_{21}}\left(\sqrt{{\tau_{21}}^2 + \left(p_{vp}^{-}\sigma_2\right)^2} + p_{vp}^{-}\sigma_2\right) + \frac{\rho_1}{\sigma_{1D}} = 1$	$\sigma_2 \geq 0\ and\ 0 \leq \left\lvert\frac{\sigma_2}{\tau_{21}}\right\rvert \leq \frac{R_{vv}^{A}}{\lvert\tau_{21c}\rvert}$
Matrix failure mode C for large transverse compression	$\left[\left(\frac{\tau_{21}}{2(1+p_{vv}^{-})S_{21}}\right)^2 + \left(\frac{\sigma_2}{Y_C}\right)^2\right]\frac{Y_C}{(-\sigma_2)} + \frac{\rho_1}{\sigma_{1D}} = 1$	$\sigma_2 \geq 0\ and\ 0 \leq \left\lvert\frac{\tau_{21}}{\sigma_2}\right\rvert \leq \frac{\lvert\tau_{21c}\rvert}{R_{vv}^{A}}$

B. OPTIMAL STRUCTURE DESIGN

To fabricate the rotor blades effectively, it is essential to identify an optimal combination of parameters that enhances structural performance, taking various design factors into account. The internal structure of the blade can be designed systematically and logically through optimization techniques that determine the choice of stacking materials, the number of layers, and the stacking angles, based on the load supported [34]. The objective function is selected based on the sensitivity identified through structural analysis, applying the optimization techniques within the defined constraints.

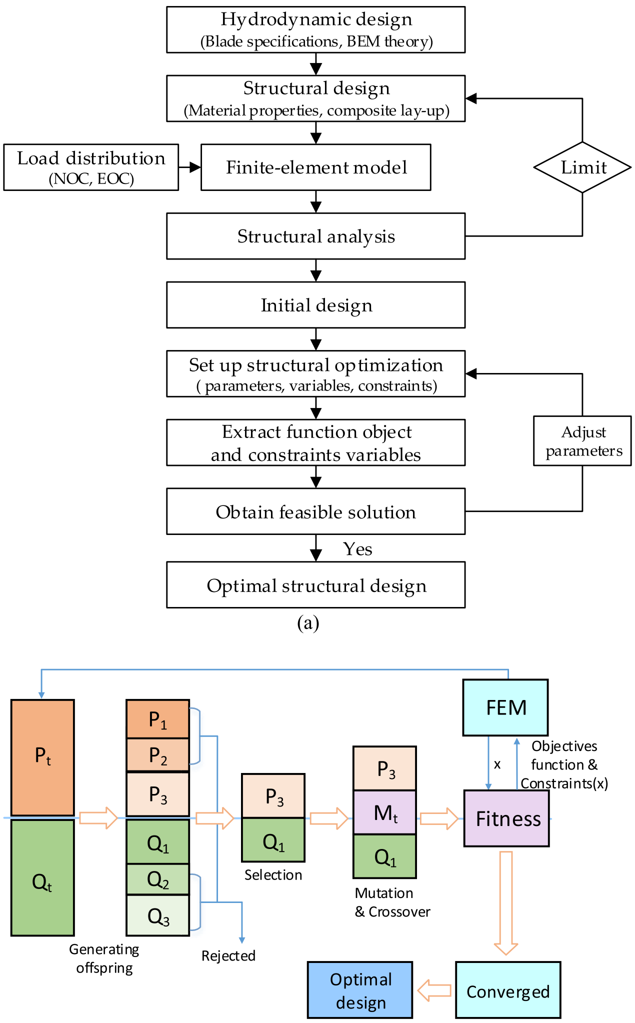

FIGURE 4. (a) Flowchart representing structural design optimization process for rotor blades; (b) Genetic algorithm process for optimization design.

Fig. 4(a) illustrates the flowchart for deriving the optimal structural design model for rotor blades used in tidal power generation. This chart displays the process of hydrodynamic design, which determines the blade's shape and output, structural design of the internal components, and a GA that adjusts design variables to find feasible solutions if the objective function exceeds the allowable range. Fig. 4(b) shows the evolution of design parameters into an optimal design model through the GA.

Thus far, the structural design of the blades has been carried out using various optimization techniques and design parameters. For instance, the thickness of the shear web, which significantly impacts structural safety, has been set as a design parameter and calculated using linear algorithms to determine tip deformations and frequencies [14], or optimized by adjusting the types of composites and fiber stacking angles [35]. Reference [29] applied topology optimization techniques to reposition the spar cap and shear web along the leading edge direction to enhance structural safety. Additionally, blade modeling has been adapted to apply the SQP optimization technique [36] across various load cases. Recently, stepwise design enhancements using GAs, simulated annealing, and particle swarm optimization have been actively utilized, with this study applying the multi-objectives genetic algorithm (MOGA) tool with NSGA-II, one of the GAs.

The GA used in this study is favored for its ability to derive feasible solutions using the Pareto frontier when multiple objective functions are present, a method widely adopted in numerous prior studies [37]. While GAs are capable of identifying optimal solutions within complex design spaces or across entire regions, their selection must be carefully selected. This is due to the constraints on design parameters that allow for practical computation times and manageable data volumes [38].

1) DESIGN PARAMETERS

The structural design optimization process used here involves utilizing a GA to refine the initially designed blade by setting design parameters, variables, and constraints, and then identifying solutions that fulfill the objective function. We established the number of layers as a design parameter, with the suction and pressure surfaces of the shell and spar cap as design variables. Constraints include tip deflection, as well as strain and stress due to fiber failure and inter-fiber failure. The objective functions were defined as the inverse reserve factor (IRF) the reciprocal of the blade safety factor and mass, aiming to determine the optimal design point that balances structural safety and mass.

$$X_S^i = \left[X_S^1, X_S^2, \cdots, X_S^n\right], \quad n = 10 \tag{15}$$

$$X_{SS}^i = \left[X_{SS}^1, \quad X_{SS}^2, \cdots, X_{SS}^n\right], \quad n = 18$$

$$X_{PS}^i = \left[X_{PS}^1, X_{PS}^2, \cdots, X_{PS}^n\right], \quad n = 2 \tag{16}$$

$$\vec{f}_{mass}(x) = min\left(\frac{m}{m_0}\right), \quad \vec{f}_{IRF}(x) < 1.0 \tag{17}$$

$$\vec{g}_t(x) \le 0.1R_{blade}, \vec{g}_\sigma(x) \le \sigma_{max}, \quad \vec{g}_\varepsilon(x) \le \varepsilon_{max} \tag{18}$$

Equations (15)–(18) detail the design parameters, variables, objective functions, and constraints. The tip deflection criteria are based on data from [26], which set the maximum tip-to-tower gap at 10% of the blade diameter, and from [14], which established the permissible tip deflection at 70% of this maximum gap. The strain and stress considerations are derived from the material's allowable limits according to the basic-geometry design values [39].

2) STACKING REDUCTION RATIO

The selection of composite materials and the arrangement of the blade's cross-section are crucial for ensuring the structural safety of the blade [15]. Even if a composite material possesses excellent elasticity and strength, employing a drop-off design method can induce stress concentration at discontinuous cross-sections.

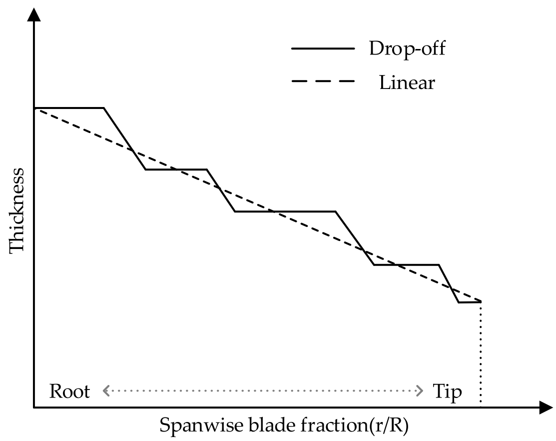

FIGURE 5. Thickness distribution along the blade for the drop-off and linear design methods.

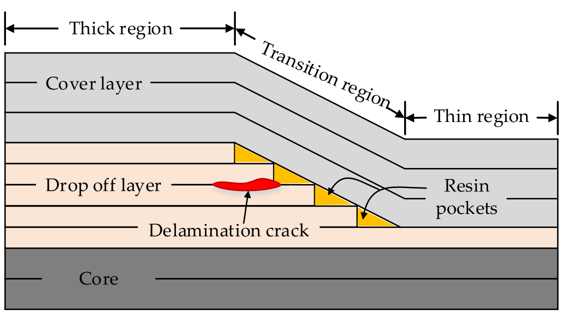

FIGURE 6. Failure and delamination cracks associated with the drop-off layered design of the composite blade section.

Fig. 5 presents the cross-sectional thickness of the blade for both drop-off and linear design methods. In the drop-off design method, transition regions arise due to abrupt changes in thickness, leading to the development of resin pockets, as shown in Fig. 6. A resin pocket is a region that reduces the strength of the composite material and can lead to delamination cracks or interfacial delamination due to load concentration. Therefore, a linear design method, which features smaller differences in thickness between cross-sections, must be applied [40].

In response, this study implemented a SRR in the spar cap to reduce failure risks associated with abrupt thickness changes. A trade-off analysis was conducted for the SRR to balance the requirements for structural safety and mass reduction by decreasing the stacking thickness at each cross-section. The SRR-based optimization of the structure used similar calculation conditions to those previously described, with the SRR designated as the design variable. The definition of the SRR is provided in (19), and the conditions for the design variable are outlined in (20).

$$SRR = \frac{Layer\ number\ of\ spar\ \ cap}{Initial\ layer\ number\ of\ spar\ cap} \tag{19}$$

$$X_L^i = \left[X_L^1, X_L^2, \cdots, X_L^n\right], \quad n = 7 \tag{20}$$

IV. RESULTS AND DISCUSSION

A. FINITE-ELEMENT MODEL AND LOAD DISTRIBUTION

The FE model of the layered blade is created using shell element 181 with a quad mesh, generating a total of 111,221 nodes to reflect the thin thickness of the layers. For the FE model of the blade, which has a 9.9 m radius and was designed using BEM theory, relative velocities and loads were assigned to each local area. The analysis for each blade element was based on the design conditions detailed in Table 1, with distributions of chord length and twist angle depicted in Fig. 7(a). The blade was divided into 10 elements along its length. The chord length measured 2.1 m at r/R = 0.2 at the blade root and tapered to 0.66 m near r/R = 1.0. The blade root, located proximal to the hub, was designed thicker to counteract flap-direction bending moments [19], while the blade tip was created thinner along the span to minimize drag effects. The twist angle, starting from r/R = 0.15, varied from 28.2° to 4.0°.

Hydrodynamic performance testing of the rotor blade revealed a power coefficient of up to 46.0% at a tip speed ratio (TSR) of 6, as shown in Fig. 7(b), achieving maximum efficiency at a rated current velocity of 2.5 m/s. This highlights the blade design's reliability and demonstrates a power coefficient that is notably high across all TSR ranges compared to previous studies.

In [30], the BEM code was utilized to analyze the performance of rotor blades for tidal power generation, yielding high performance coefficients even at low current velocities. Reference [41] reports the design and analysis of 1-MW- class blades using the hydrofoil S814, achieving a performance efficiency of up to 47.6 %.

Although the results of the current study and those in [41] showed similar trends overall, the performance coefficient in [41] experienced significant decreases at both low and high current velocity ranges. This variation was attributed to differences in the current inflow angle owing to the rated TSR and optimization strategies employed. Conversely, in [42], despite the blades having the same rated capacity, the performance coefficient showed heightened sensitivity to variations in current velocity when two turbine blades were implemented. Fig. 8(a) depicts a three-dimensional model of a tidal current turbine rotor blade designed using BEM theory. It shows both the outer shell and internal structures, including the spar cap and shear web. The finite-element model is

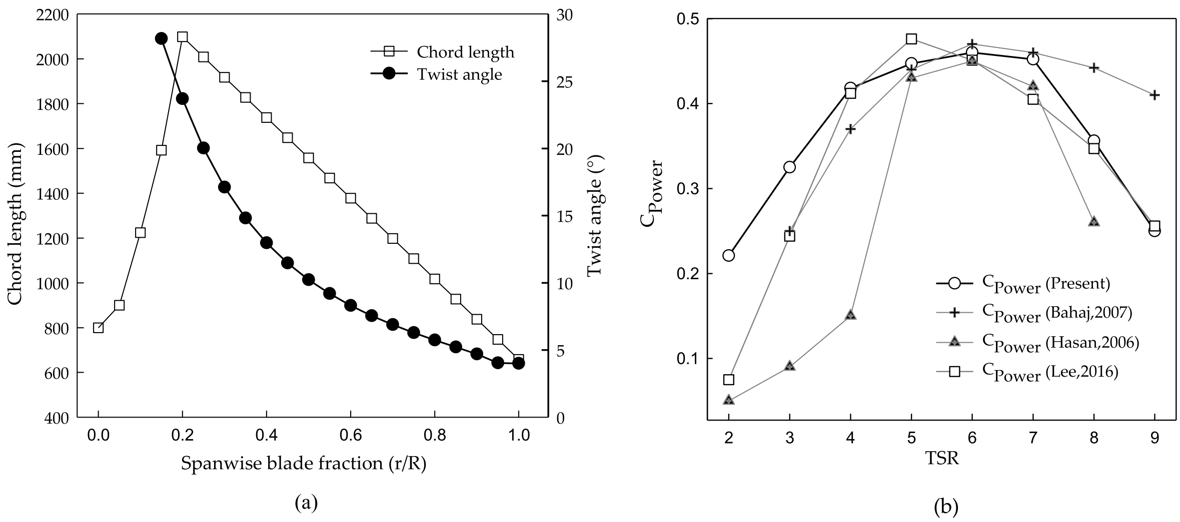

FIGURE 7. (a) Distributions of the chord length and twist angle with respect to the spanwise blade fraction. (b) Comparison of power coefficients for 1-MW tidal current turbines.

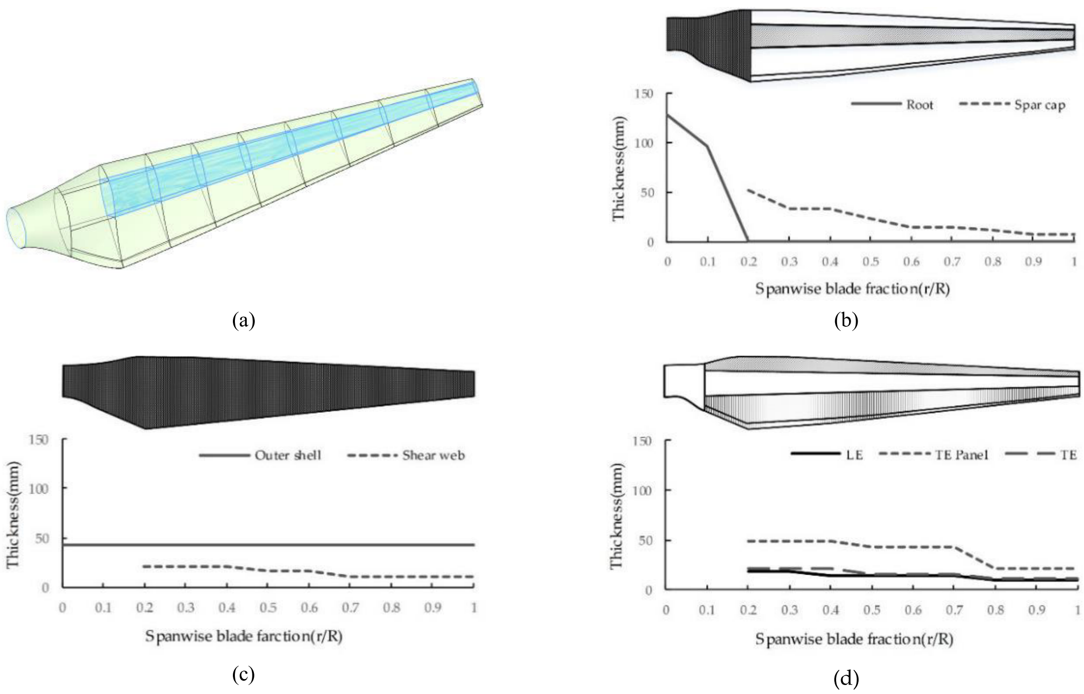

FIGURE 8. Configuration initial geometry and distribution of thickness for rotor blade. (a) 3-dimensional initial geometry. (b) Root, spar cap. (c) Shell, shear web. (d) LE, TE panel, TE.

divided for stacking based on the structural characteristics. Fig. 8(b)–(d) illustrate the arrangement of the internal structure and the stacking thickness for the basic blade. The blade structure design in this study is informed by the wind turbine blade designs presented in [43] and incorporates elements of tidal current turbine blade design, including rear shear webs at 15% and 50% of the chord length in each cross-section as noted in [10]. The calculation of flow-induced loads is crucial in the structural design of turbine blades, with structural safety assessed by predicting load conditions and assigning specific load values. In this study, the loads applied to the finite-element model were categorized under normal operating conditions (NOC)—specifically, the rated current velocity of 2.5 m/s as proposed by [20] and extreme operating conditions (EOC), where a partial load factor of 1.35 as proposed by the IEC [44] was considered. These loads vary in both direction and magnitude across different sections of the blade surface and are thus assigned locally. They can be classified into axial forces, which act perpendicularly to the blade surface and are significantly influenced by blade rotation [20], and tangential forces, which act parallel to the blade surface, generating torque and power.

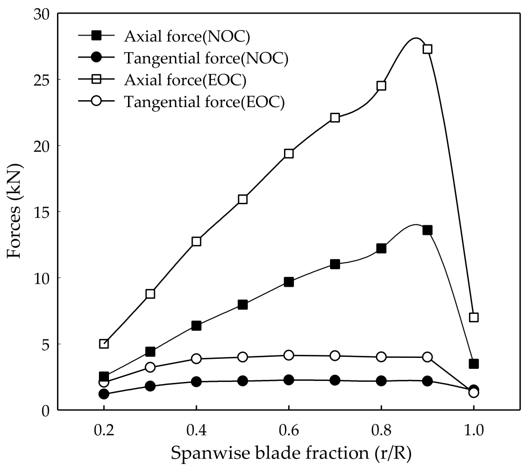

FIGURE 9. Axial and tangential force distributions with respect to the spanwise blade fraction.

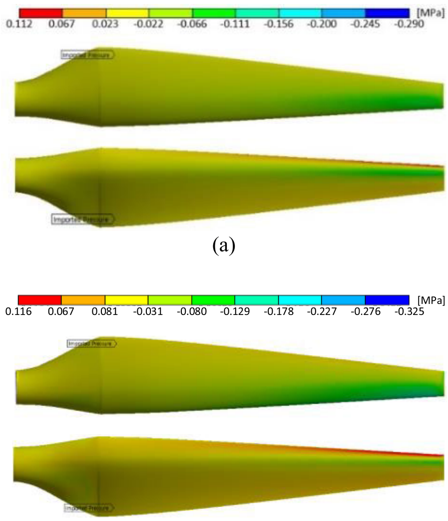

FIGURE 10. Pressure distributions for the blade surface: (a) NOC; (b) EOC.

Fig. 9 illustrates the distribution of loads on the blade surface under both NOC and EOC, with axial and tangential forces reaching maximum values of 27.3 kN and 4.1 kN, respectively. Although these forces are initially calculated locally, they are applied to the blade surface using the equivalent static load distribution method. For structural failure evaluations, however, these forces are transformed into a spatial distribution load across the blade surface, as depicted in Fig. 10 [45].

The FE model of the structurally designed blade is highly complex, and results vary depending on grid conditions [46]. Therefore, to enhance the accuracy of the FE model's results, modeling was performed according to the grid size as shown in Table 5, and grid dependency was evaluated by comparing numerical results. The reference grid size was set in the range of 10-35 mm, and trends in strain and IRF according to grid conditions are shown in Fig. 11. Models with more than 110,000 nodes and a reference grid size of 25 mm exhibited a consistent trend in converging results. Consequently, a reference grid size of 25 mm was selected for conducting this study.

TABLE 5. Grid configuration of fe model conditions.

Grid size (mm)	Type of grids	Nodes	Elements
35	Quad/ Triangular	81,663	82,279
30		92,728	93,336
25		111,221	111,819
20		144,892	145,497
15		219,103	219,676
10		436,579	437,140

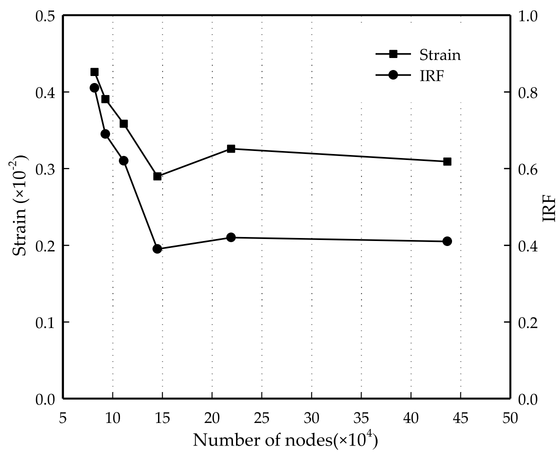

FIGURE 11. Grid independence test of the FE model.

B. STRUCTURAL LOAD ANALYSIS

The mechanical loads induced by blade rotation can lead to the failure of composite materials, necessitating structural validation of the finite-element modeling [47]. In this study, the 9.9 m rotor blade was considered to be at risk of failure when the IRF failure index reached or exceeded 1, based on the strain and stress metrics from the limit criterion and the theories of the interaction criterion and separation mode criterion. Given that the spar cap primarily supports the vertical and axial forces exerted on the blade, the failure potential of the entire blade was evaluated based on the structural properties of the spar cap [44].

Fig. 12 displays the strain and stress on the suction and pressure surfaces of the spar cap under the NOC and EOC. It illustrates the dimensionless strain of the spar cap, normalized against the maximum strain value observed in the blade. The strain readings on the pressure and suction surfaces are positive and negative, respectively, reflecting the tension and compression induced by the loads [19]. Near the root, both surfaces of the spar cap exhibit significant strain,

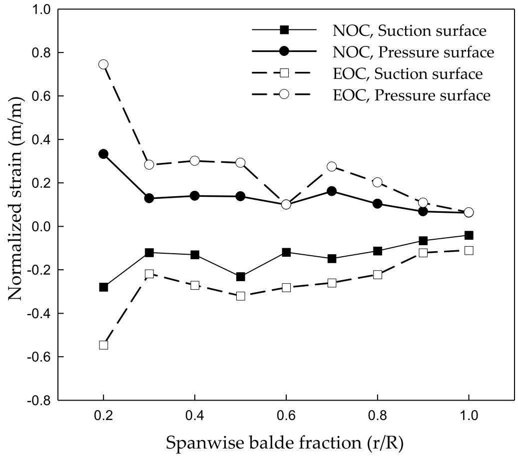

(a)

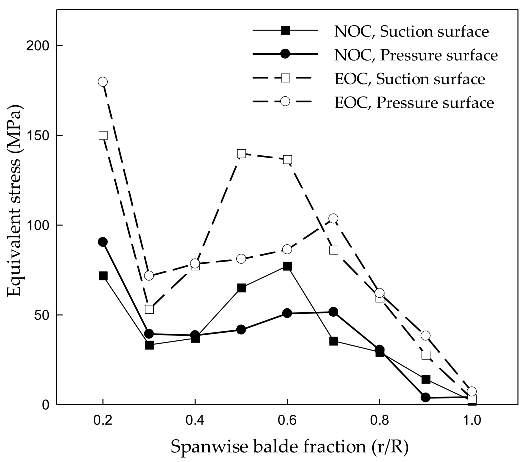

(b)

FIGURE 12. Distributions of the (a) maximum normalized strain and (b) equivalent stress on the spar cap surface under various operating conditions.

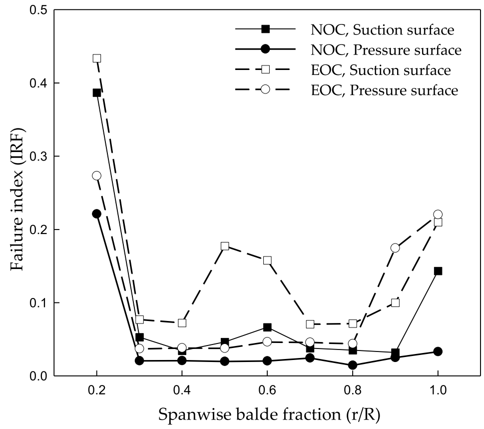

(a)

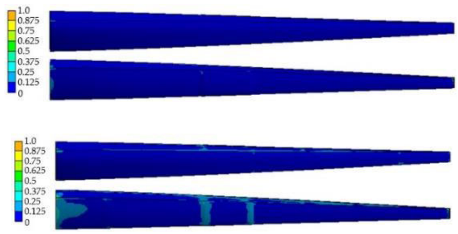

(b)

FIGURE 13. (a) Distributions of the failure index and (b) failure index contours on the spar cap surface under various operating conditions.

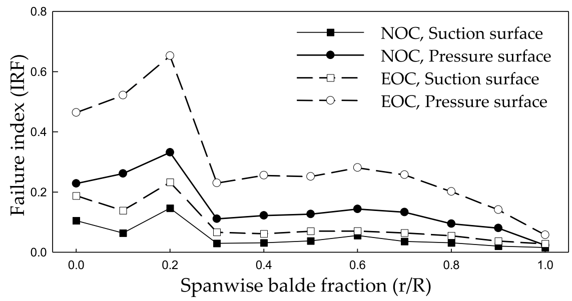

(a)

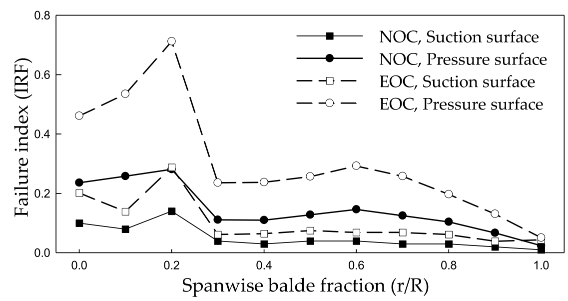

(b)

FIGURE 14. Distribution of the failure index on the blade surface with respect to the spanwise blade fraction: (a) Tsai-Wu's failure criteria; (b) Puck's failure criteria.

which rapidly diminishes past r/R = 0.2, where the spar cap is positioned. Notably, the strain is generally higher on the pressure surface compared to the suction surface owing to the effects of blade rotation and edge-direction deformation. The strain patterns under NOC closely resemble those under EOC, indicating minimal structural deformation. However, under EOC conditions, the maximum strain at r/R = 0.2 on the suction surface reached 0.74. Similarly, stress in the spar cap peaked near the root and decreased toward the tip. However, between r/R = 0.4 and 0.6, a significant increase in stress on the suction surface suggests the impact of flow-induced loads on the thinner sections of the spar cap.

The failure of the blade spar cap, made from an anisotropic material, was assessed using Tsai-Wu's failure theory, with the results depicted in Fig. 13. The failure index of the spar cap mirrored the stress patterns; however, the strain was more pronounced on the suction surface than on the pressure surface [5]. Additionally, as illustrated in Fig. 13(b), the failure index increased notably at points where the thickness of the spar cap changed abruptly at the interface with the structure. Hence, it is crucial to minimize changes in thickness resulting from both the stacking design and the material properties. This finding aligns with those in [9], affirming the structural

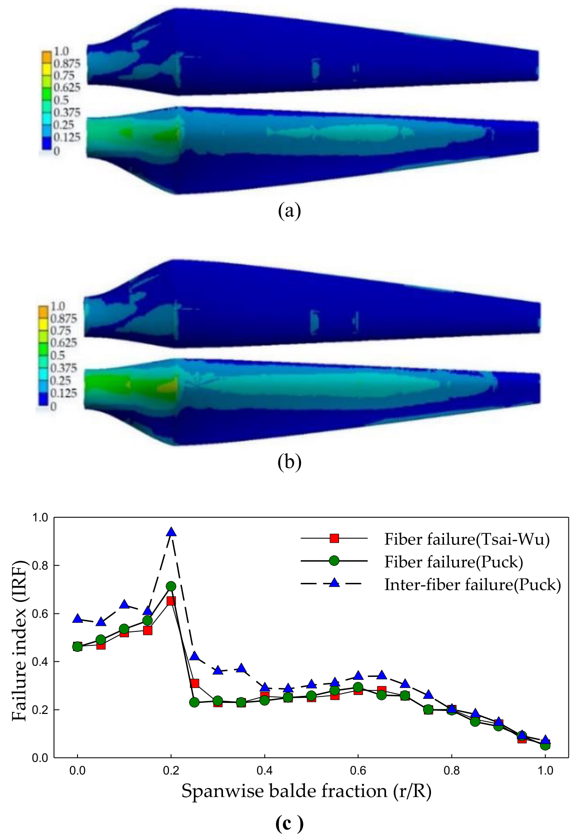

FIGURE 15. Failure-criterion results for fiber failure and inter-fiber failure under EOC: (a) Puck's fiber failure surface contour, with $IRF_{MAX} = 0.712$; (b) Puck's inter-fiber failure surface contour, with $IRF_{MAX} = 0.935$; (c) distributions of fiber failure and inter-fiber failure.

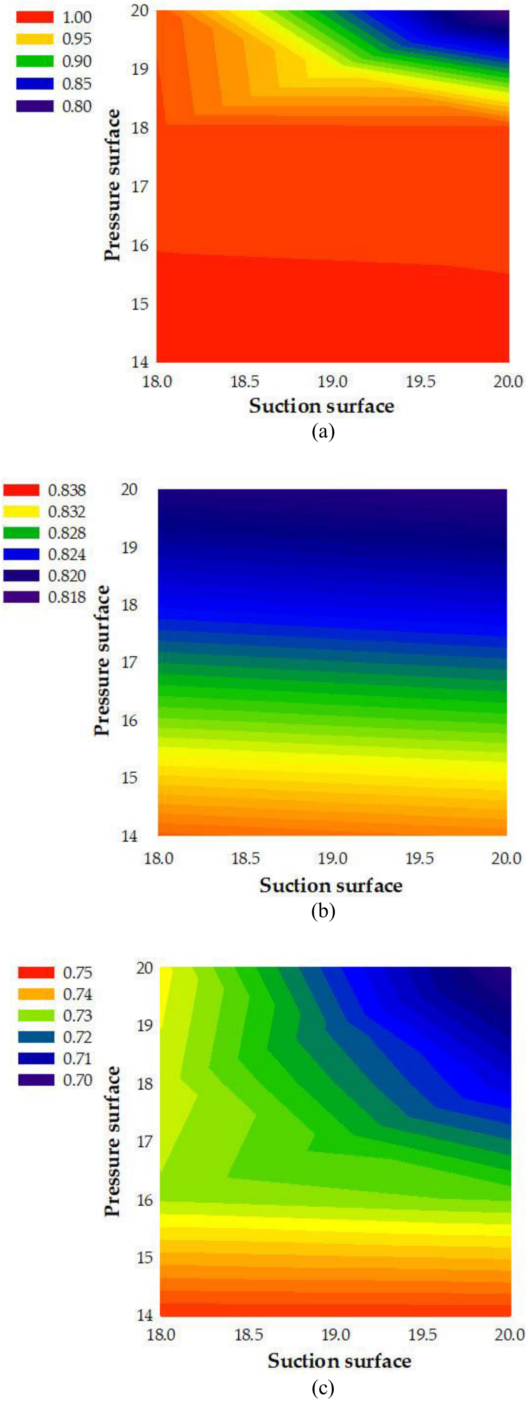

FIGURE 16. Surface plots of the IRF for different numbers of layers on the shell: (a) $X_S^i = 5$; (b) $X_S^i = 6$; (c) $X_S^i = 7$.

integrity. To ascertain the failure modes of the blade fibers, we evaluated the failure indices using the failure criteria of Tsai-Wu and Puck. Fig. 14 shows the failure index along the span; notably, there is no indication of failure across the blade, although the maximum values of the IRF vary.

For the inter-fiber failure mode, the analysis involved calculating the transverse tensile stress, transverse compressive stress, and compressive stress acting on the fibers. Inter-fiber failure was noted in each mode when the stresses and shear forces exceeded the allowable limits. Fig. 15 indicates that, for fiber failure, the Tsai-Wu failure mode resulted in an IRF_{max} of 0.653, while the Puck failure mode led to an IRF_{max} of 0.712. In the case of Puck's inter-fiber failure mode, the IRF_{max} reached 0.935. Both fiber and inter-fiber failures predominantly occurred near the root, with inter-fiber failure indices also rising in the middle section of the blade. However, in all analyzed conditions, the failure index did not exceed 1, indicating that no failures occurred.

C. OPTIMAL STRUCTURAL DESIGN MODEL

To enhance the structural design of the blade, the parameters X_S^i, X_{SS}^i, and X_{PS}^i, known to significantly influence structural safety, were selected as the design variables. Fig. 16 illustrates the distribution of the failure index, calculated by setting upper and lower bounds for X_{SS}^i and X_{PS}^i. Application of the Puck failure criterion revealed that the failure index surpassed 1 at $X_S^i = 5$, indicating blade failure. Notably, this failure occurred irrespective of the number of layers on the suction and pressure surfaces of the spar cap.

Fig. 16(b) displays the failure index distribution at $X_S^i = 6$ for the shell, which exhibited a maximum of 0.834.

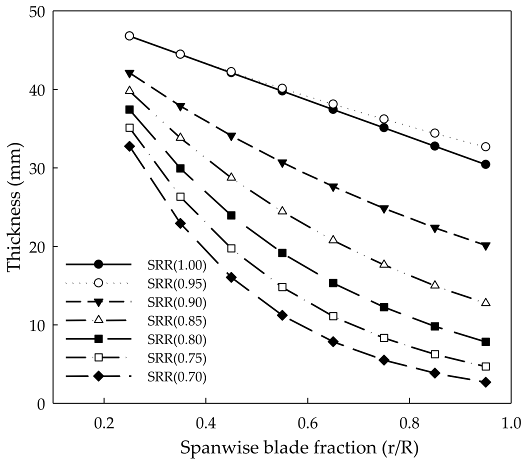

FIGURE 17. Distribution of the layer thickness with respect to the spanwise blade fraction.

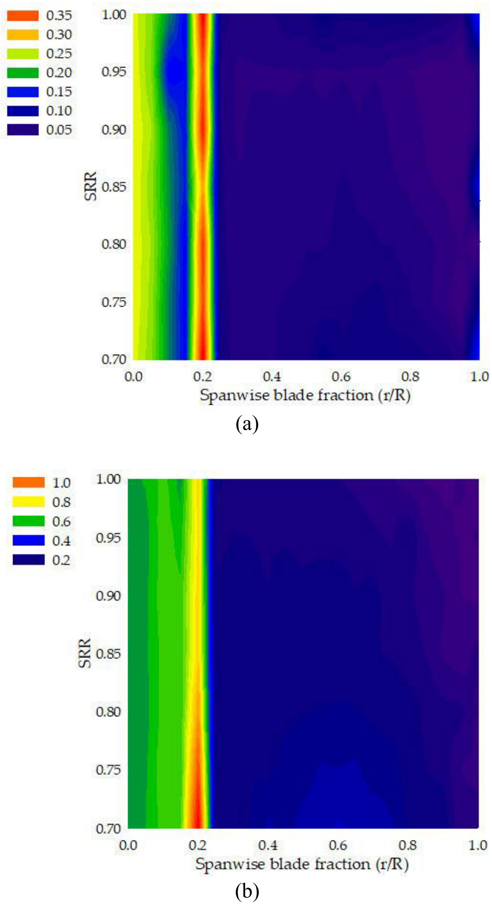

FIGURE 18. Distribution of the failure index on the blade surface with respect to the SRR: (a) suction surface; (b) pressure surface.

The highest value of the failure index was observed at $X_{PS}^{i} = 14$, with elevated indices across all regions regardless of X_{SS}^{i}. This pattern suggests that the failure index is more sensitive to variations in the number of layers on the pressure surface of the spar cap than on the suction surface. The failure index distribution at $X_{S}^{i} = 7$ exhibited characteristics of both the distributions at $X_{S}^{i} = 5$ and $X_{S}^{i} = 6$. At $X_{PS}^{i} = 14$, the maximum failure index remained 0.75, irrespective of the layer count on the suction surface. However, in regions where X_{PS}^{i} reached 16 or higher, the failure index was dependent on the number of layers on the suction surface. The sloping curve between the suction and pressure surfaces approached feasible solutions, revealing a visible Pareto frontier. Within this frontier, the balance between structural safety and economic efficiency was evaluated to identify potential feasible solution candidates.

The SSR of the blade spar cap was established within a range of 0.7 to 1.0, with increments of 0.05. Fig. 17 illustrates the distribution of cross-sectional thickness relative to the SRR. Under this setting, the reduction was more pronounced in the initial spar cap layers on both the suction and pressure surfaces, and the spar cap was thicker at the blade tip for an SRR of 0.95 compared to an SRR of 1.0. The failure of the blade surfaces, assessed using the Puck failure criterion, is presented in Fig. 18. Across both the suction and pressure surfaces of the blade, the highest failure index was observed at approximately r/R = 0.2 in the longitudinal direction of the blade [14], [22], [24], with only minor variations in the failure index toward the blade tip.

On the suction surface, the peak failure index reached 0.389, while on the pressure surface, it surpassed 1.0 at an SRR of 0.75, peaking at 1.15 around r/R = 0.2, which indicates potential failure of the blade. Consequently, an SRR of at least 0.8 is recommended to maintain structural safety. Additionally, there was a noticeable difference in the trajectory of the failure index reaching its maximum value between the suction and pressure surfaces in the section from r/R = 0 to 0.2. On the suction surface, the failure index decreased after the root section before reaching its maximum, whereas on the pressure surface, it increased gradually to its maximum value. This variation in the failure index can be attributed to the bending of the blade, which imposes tensile loads on the suction surface and compressive loads on the pressure surface, thereby affecting the failure indices differently.

Fig. 19 illustrates the distribution of the failure index on the pressure surface of the blade in relation to the SRR of the spar cap. As previously noted, the bending load often leads to a high failure index near the interface between the blade root and the spar cap, attributable to stress concentration from the abrupt change in layer thickness at the root and spar cap. Moreover, with an SRR of 0.7, there is a noticeable increase in the failure index in the mid-board region as the SRR decreases.

Fig. 20 provides a three-dimensional view of the failure index along the span of the blade's pressure surface concerning the SRR. It demonstrates that the failure index begins to exceed 1 around an SRR of 0.75.

Fig. 21 displays the distribution of the IRF results for models generated through the design optimization process, which varied across different design parameters, including SRRs.

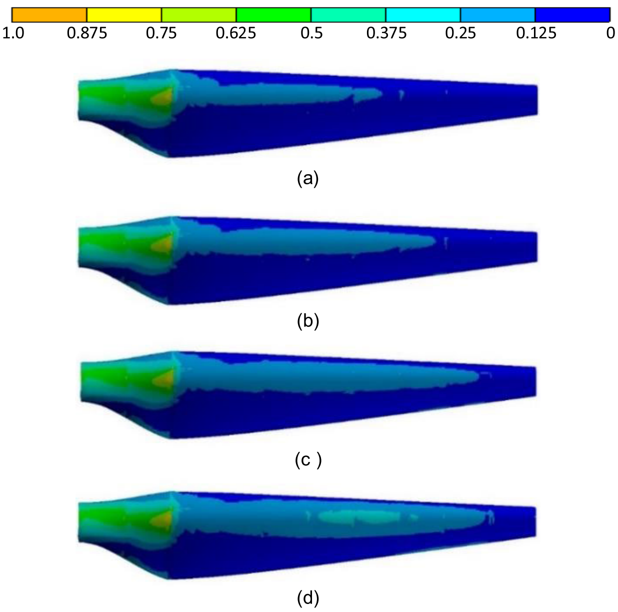

FIGURE 19. Distribution of the failure index on the pressure surface: (a) SRR = 1.0; (b) SRR = 0.9; (c) SRR = 0.8; (d) SRR = 0.7.

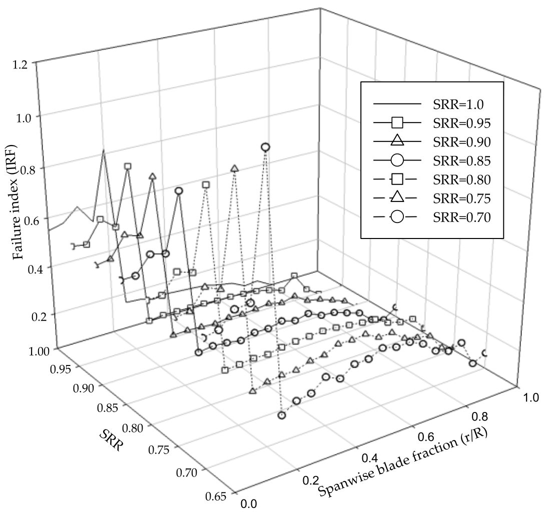

FIGURE 20. Distribution of the failure index on the spar-cap surface under various operating conditions.

The models identified as optimal candidates incorporated mass and failure index as objective functions. The Pareto principle was applied to show the feasible-solution surface that concurrently satisfies multiple objective functions. From this surface, three models were selected based on a rational allocation of structural performance indicators such as tip deflection, strain, stress, failure index, and mass. Table 6 details these performance indicators. Optimal model A exhibited the best tip deflection and failure index metrics; however, it was the heaviest among the candidates. Thus, the weightings assigned to the variables in this model differed significantly from those in optimal model C. Notably, the mass of optimal model C was 2420 kg, approximately 23.6% lighter than the total blade mass of 3169 kg for the basic geometry (initial model).

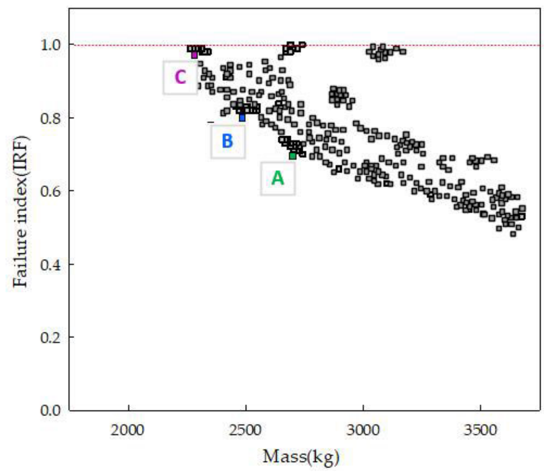

FIGURE 21. Results of optimal model.

TABLE 6. Structural performance for initial and optimal models.

Design	Tip deflection (mm)	Max. strain (mm/mm)	Max. stress (MPa)	Failure index (IRF)	Total mass (kg)
Initial model	233	0.0001838	5.24	0.44	3169
Optimal model A	364	0.0043925	13.75	0.67	2742
Optimal model B	374	0.0050752	17.08	0.78	2250
Optimal model C	416	0.0053634	18.31	0.92	2420

V. CONCLUSION

In this study, the design of a rotor blade for a tidal current turbine focused on ensuring structural safety under extreme conditions. A finite-element model was utilized to analyze potential failures, and a GA was applied to optimize the structural design based on targeted objective functions. The study yielded the following conclusions:

(1) The blade, designed with a 19.8 m diameter based on hydrodynamic performance analyses according to BEM theory, achieved a maximum performance coefficient of 44.8-% at a rated current velocity of 2.5 m/s. Structural integrity was enhanced by employing a lamination process that incorporated both GFRP and CFRP.

(2) The structural safety of the blade was assessed using the finite-element model. Particularly the spar cap, which supports the majority of the load, revealed maximum stress and strain concentrations at r/R = 0.2 under EOC, with notable changes on the pressure surface. Additionally, the application of Tsai-Wu's and Puck's failure indices confirmed that the

IRF did not exceed 1, substantiating the absence of both fiber and inter-fiber failures.

(3) The suction and pressure surfaces of the shell and spar cap were designated as design parameters. An optimal design point was determined using GA, with the failure index and mass serving as objective functions, subject to various constraints. Specifically, when optimizing the number of layers on the shell, conditions were set to avoid exceeding the limits for tip deflection, strain, stress, and the failure index. The failure index surpassed 1 at $X_S^i = 5$, indicating potential overall failure regardless of the layer count on the suction and pressure surfaces of the spar cap. Notably, a Pareto region between these surfaces was identified at $X_S^i = 7$.

(4) To avoid stress concentration caused by rapid changes in layer thickness within the spar cap, a tradeoff analysis was conducted. This analysis aimed to balance structural safety and mass reduction by utilizing the SRR as a design variable. Below an SRR of 0.75, the failure index exceeded 1 at approximately r/R = 0.2 and failed to align with the objective functions. Additionally, variations in the failure index, influenced by tensile and compressive loads on the spar cap owing to blade bending, were observed.

(5) Optimal model candidates were derived based on changes in design parameters and SRR, guided by the objective functions of mass and failure index. These candidates were distributed effectively across the feasible-solution surface according to the performance indicators. The optimal model was selected by weighting the tip deflection, failure index, and mass, achieving a mass reduction of approximately 23.6 % compared to the basic geometry (initial model).

This study has successfully identified an optimal design point that accommodates multiple design parameters and meets quantified objectives, effectively balancing constraints with the objectives of mass reduction and failure index management. In future studies, the optimization design process established using a genetic algorithm and the distribution characteristics of the failure index will be utilized to design an optimization model for each fraction of the blade. Furthermore, a prototype composite blade will undergo a load test.

REFERENCES

[1] N. Safari, S. M. Mazhari, B. Khorramdel, and C. Y. Chung, ''Tidal current and level uncertainty prediction via adaptive linear programming,'' *IEEE Trans. Sustain. Energy*, vol. 10, no. 2, pp. 748–758, Apr. 2019.

[2] C.-H. Jo, K.-H. Lee, S.-J. Hwang, and D.-Y. Kim, ''Performance analysis of 200kW tidal current power turbine with pre-deformed blades,'' in *Proc. IEEE 15th Int. Conf. Environ. Electr. Eng. (EEEIC)*, Rome, Italy, Jun. 2015, pp. 472–477.

[3] J. Chen, X. Shen, X. Zhu, and Z. Du, ''Study on composite bend-twist coupled wind turbine blade for passive load mitigation,'' *Composite Struct.*, vol. 213, pp. 173–189, Apr. 2019.

[4] H. Ullah and V. V. Silberschmidt, ''Analysis of impact induced damage in composites for wind turbine blades,'' in *Proc. Power Gener. Syst. Renew. Energy Technol. (PGSRET)*, Islamabad, Pakistan, Jun. 2015, pp. 1–6.

[5] Q. D. Nguyen, H. C. Park, T. Kang, and J. H. Ko, ''Structural design and analysis of composite blade for horizontal-axis tidal turbine,'' *Sci. Eng. Composite Mater.*, vol. 25, no. 6, pp. 1075–1083, Nov. 2018.

[6] D. M. Grogan, S. B. Leen, C. R. Kennedy, and C. M. Brádaigh, ''Design of composite tidal turbine blades,'' *Renew. Energy*, vol. 57, pp. 151–162, Sep. 2013.

[7] M. Calvario, L. S. Sutherland, and C. G. Soares, ''A review of the applications composite materials in wave and tidal energy devices,'' in *Proc. 17th Int. Mari. Asso. Medit (IMAM)*, 2017, pp. 1111–1117.

[8] M. H. Somoza, T. Macquart, and A. Maheri, ''Reduction of tidal turbines hydrodynamic loads employing bend-twist adaptive blades,'' in *Proc. 3rd Int. Symp. Environ. Friendly Energies Appl. (EFEA)*, Paris, France, Nov. 2014, pp. 1–5.

[9] R. H. Barnes, E. V. Morozov, and K. Shankar, ''Evaluation of simplified loading models for finite element analysis of composite wind turbine blades,'' in *Proc. Int. Conf. Compos. Mater. (ICCM)*, Copenhagen, Denmark, Jul. 2015, pp. 1–3.

[10] G. S. Bir, M. J. Lawson, and Y. Li, ''Structural design of a horizontal-axis tidal current turbine composite blade,'' in *Proc. ASME 30th Int. Conf.*, Jun. 2011, pp. 19–24.

[11] R. Liao, Y. He, T. Feng, X. Yang, W. Dai, and W. Zhang, ''Mission reliability-driven risk-based predictive maintenance approach of multi-state manufacturing system,'' *Rel. Eng. Syst. Saf.*, vol. 236, Aug. 2023, Art. no. 109273.

[12] K. Hayat and S. K. Ha, ''Load mitigation of wind turbine blade by aeroelastic tailoring via unbalanced laminates composites,'' *Composite Struct.*, vol. 128, pp. 122–133, Sep. 2015.

[13] M. Fal, R. Hussein, K. Chandrashekhara, A. Abutunis, and V. Menta, ''Experimental and numerical failure analysis of horizontal axis water turbine carbon fiber-reinforced composite blade,'' *J. Renew. Sustain. Energy*, vol. 13, no. 1, Jan. 2021, Art. no. 014501.

[14] Z. Zhang, C. Zhang, Y. Qiao, Y. Zhou, and S. Wang, ''Design and mass optimization of numerical models for composite wind turbine blades,'' *J. Mar. Sci. Eng.*, vol. 11, no. 1, p. 75, Jan. 2023.

[15] C.-S. Lee and J.-M. Lee, ''A study on the evaluation of fiber and matrix failures for laminated composites using Hashin·Puck failure criteria,'' *J. Soc. Nav. Architects Korea*, vol. 52, no. 2, pp. 143–152, Apr. 2015.

[16] S. E. Hosseini, O. Karimi, and M. A. AsemanBakhsh, ''Experimental investigation and multi-objective optimization of savonius wind turbine based on modified non-dominated sorting genetic algorithm-II,'' *Wind Eng.*, vol. 48, no. 3, pp. 446–467, Dec. 2023.

[17] M. H. Shojaeefard, S. E. Hosseini, and J. Zare, ''CFD simulation and Pareto-based multi-objective shape optimization of the centrifugal pump inducer applying GMDH neural network, modified NSGA-II, and TOPSIS,'' *Structural Multidisciplinary Optim.*, vol. 60, no. 4, pp. 1509–1525, May 2019.

[18] J. H. VanZwieten, N. Vanrietvelde, and B. L. Hacker, ''Numerical simulation of an experimental ocean current turbine,'' *IEEE J. Ocean. Eng.*, vol. 38, no. 1, pp. 131–143, Jan. 2013.

[19] W. Finnegan, Y. Jiang, P. Meier, L. C. Hung, E. Fagan, F. Wallace, C. Glennon, M. Flanagan, T. Flanagan, and J. Goggins, ''Numerical modelling, manufacture and structural testing of a full-scale 1 MW tidal turbine blade,'' *Ocean Eng.*, vol. 266, Dec. 2022, Art. no. 112717.

[20] H. Gonabadi, A. Oila, A. Yadav, and S. Bull, ''Structural performance of composite tidal turbine blades,'' *Composite Struct.*, vol. 278, Dec. 2021, Art. no. 114679.

[21] A. D. Hoang and C.-J. Yang, ''Design and performance evaluation of a 10kW scale counter-rotating wind turbine rotor,'' *J. Korean Soc. Mar. Environ. Saf.*, vol. 20, no. 1, pp. 104–112, Feb. 2014.

[22] J. L. Tangler and D. M. Somers, ''NREL airfoil families for HAWTs,'' Nat. Renew. Eenergy Lab., Golden, CO, USA, Tech. Rep. NREL/TP-442–7109, 1995, pp. 2–4. [Online]. Available: https://www.nrel.gov/docs/legosti/old/7109.pdf

[23] M. Nuernberg and L. Tao, ''Experimental study of wake characteristics in tidal turbine arrays,'' *Renew. Energy*, vol. 127, pp. 168–181, Nov. 2018.

[24] M. Hannon. (2016). *World Energy Resources Marine Energy*. World Energy Council. [Online]. Available: http://large.stanford.u/courses/2018/ph240/rogers2/docs/wec-2016.pdf

[25] A. Boretti, ''State-of-the-art of MW-level capacity oceanic current turbines,'' *Nonlinear Eng.*, vol. 9, no. 1, pp. 361–369, Aug. 2020.

[26] B. S. Kim, ''Multi-MW class wind turbine blade design part I : Aerostructure design and integrated load analysis,'' *Trans. Korean Soc. Mech. Eng. B*, vol. 38, no. 4, pp. 289–309, Apr. 2014.

[27] M. S. Kumar, A. S. Krishnan, and R. Vijayanandh, ''Vibrational fatigue analysis of NACA 63215 small horizontal axis wind turbine blade,'' in *Proc. Int. Conf. Emerg. Trends Mater. Manuf. Eng. (IMME)*, Mar. 2017, pp. 6665–6674.

[28] J. Joustra, B. Flipsen, and R. Balkenende, ''Structural reuse of high end composite products: A design case study on wind turbine blades,'' *Resour., Conservation Recycling*, vol. 167, Apr. 2021, Art. no. 105393.

[29] L.-C. Forcier and S. Joncas, ''Development of a structural optimization strategy for the design of next generation large thermoplastic wind turbine blades,'' *Struct. Multidisciplinary Optim.*, vol. 45, no. 6, pp. 889–906, Dec. 2011.
[30] A. S. Bahaj, A. F. Molland, J. R. Chaplin, and W. M. J. Batten, ''Power and thrust measurements of marine current turbines under various hydrodynamic flow conditions in a cavitation tunnel and a towing tank,'' *Renew. Energy*, vol. 32, no. 3, pp. 407–426, Mar. 2007.
[31] W. Finnegan, Y. Jiang, N. Dumergue, P. Davies, and J. Goggins, ''Investigation and validation of numerical models for composite wind turbine blades,'' *J. Mar. Sci. Eng.*, vol. 9, no. 5, p. 525, May 2021.
[32] G. Park, C. Kong, H. Lee, and H. Park, ''A study on design of 500W class high efficiency horizontal axis wind turbine system(HAWTS) blade using natural fiber composites,'' *Composites Res.*, vol. 28, no. 3, pp. 104–111, Jun. 2015.
[33] A. Puck and H. Schürmann, ''Failure analysis of FRP laminates by means of physically based phenomenological models,'' *Composites Sci. Technol.*, vol. 58, no. 7, pp. 1045–1067, Jul. 1998.
[34] K. Hayat and S. K. Ha, ''Flutter performance of large-scale wind turbine blade with shallow-angled skins,'' *Composite Struct.*, vol. 132, pp. 575–583, Nov. 2015.
[35] S. Jelena, T. Zorana, B. Marija, and P. Ognjen, ''Rapid multidisciplinary, multi-objective optimization of composite horizontal-axis wind turbine blade,'' in *Proc. Int. Conf. Multidisciplinary Eng. Design Optim. (MEDO)*, Belgrade, Serbia, Sep. 2016, pp. 1–6.
[36] J. Jasa, P. Bortolotti, D. Zalkind, and G. Barter, ''Effectively using multifidelity optimization for wind turbine design,'' *Wind Energy Sci.*, vol. 7, no. 3, pp. 991–1006, May 2022.
[37] E. J. Yeo, D. M. Kennedy, and F. O'Rourke, ''Tidal current turbine blade optimisation with improved blade element momentum theory and a non-dominated sorting genetic algorithm,'' *Energy*, vol. 250, Jul. 2022, Art. no. 123720.
[38] R. Özkan and M. S. Genç, ''Multi-objective structural optimization of a wind turbine blade using NSGA-II algorithm and FSI,'' *Aircr. Eng. Aerosp. Technol.*, vol. 93, no. 6, pp. 1029–1042, Aug. 2021.
[39] K. Y. Maalawi and H. M. Negm, ''Optimal frequency design of wind turbine blades,'' *J. Wind Eng. Ind. Aerodynamics*, vol. 90, no. 8, pp. 961–986, Aug. 2002.
[40] L. Mishnaevsky, ''Root causes and mechanisms of failure of wind turbine blades: Overview,'' *Materials*, vol. 15, no. 9, p. 2959, Apr. 2022.
[41] K. H. Lee, ''Analysis of horizontal axis tidal turbine performance and turbine efficiency deficit from blade deformation,'' Ph.D. dissertation, Dept. Naval Architecture and Ocean Engineering, Inha Univ., Incheon, South Korea, 2016.
[42] H. Yazicioglu, K. M. M. Tunc, M. Ozbek, and T. Kara, ''Simulation of electricity generation by marine current turbines at Istanbul bosphorus strait,'' *Energy*, vol. 95, pp. 41–50, Jan. 2016.
[43] D. T. Griffith and T. D. Ashwill, ''The Sandia 100-meter all-glass baseline wind turbine blade: SNL100–00,'' Sandia Nat. Laboratories, Tech. Rep. SAND2011–3779, 2011. [Online]. Available: https://energy.sandia.gov/wp-content/gallery/uploads/113779.pdf
[44] Y. Jiang, W. Finnegan, F. Wallace, M. Flanagan, T. Flanagan, and J. Goggins, ''Structural analysis of a 1 MW tidal turbine blade through full-scale physical testing and a digital twin,'' in *Proc. MARINE*, Jun. 2021, pp. 2–4.
[45] J. Berg, J. Paquette, and B. Resor, ''Mapping of 1D beam loads to the 3D wind blade for buckling analysis,'' in *Proc. 52nd AIAA/ASME/ASCE/AHS/ASC Struct., Structural Dyn. Mater. Conf.*, Apr. 2011, p. 1880.
[46] B. Lopes, M. R. T. Arruda, L. Almeida-Fernandes, L. Castro, N. Silvestre, and J. R. Correia, ''Assessment of mesh dependency in the numerical simulation of compact tension tests for orthotropic materials,'' *Compos. C, Open Access*, vol. 1, Aug. 2020, Art. no. 100006.
[47] P. M. Singh and Y.-D. Choi, ''Shape design and numerical analysis on a 1 MW tidal current turbine for the south-western coast of Korea,'' *Renew. Energy*, vol. 68, pp. 485–493, Aug. 2014.

HAECHANG JEONG (Member, IEEE) received the B.S. degree in marine engineering from Mokpo National Maritime University, Mokpo, South Korea, in 2010, and the M.S. and Ph.D. degrees in mechanical engineering from Mokpo National Maritime University, in 2017 and 2023, respectively. From 2010 to 2015, he was a Senior Engineer with Hanjin Shipping Company Ltd., Busan. He is currently a Senior Engineer with T/S Saenuri, Mokpo National Maritime University. His research interests include the improvement of power performance for conversion devices, marine renewable energy resource assessment, and optimization of structural design.

CHANGJO YANG received the B.S. degree in marine engineering and the M.S. degree in mechanical engineering from Korea Maritime and Ocean University, Busan, South Korea, in 1993 and 1999, respectively, and the Ph.D. degree in mechanical engineering from Kyushu Institute of Technology, Kyushu, Japan, in 2004.

From 2004 to 2006, he was a Lecturer with Kyushu Institute of Technology. Since April 2006, he has been a Professor with the Department of Marine Engineering, Mokpo National Maritime University. His research interests include modeling, marine renewable energy resource assessment, and design and type-certification of marine energy conversion technologies. He is a member and a Subject Matter Expert of the International Electrotechnical Commission (IEC), developing international standards for the marine renewable energy industry.